Image and Vision Computing 28 (2010) 614–625

Contents lists available at ScienceDirect

Image and Vision Computing

journal homepage: www.elsevier.com/locate/imavis

Segmentation of the carotid intima-media region in B-mode ultrasound images

Rui Rocha [a,b,*], Aurélio Campilho [a,c], Jorge Silva [a,c], Elsa Azevedo [d,e], Rosa Santos [e]

[a] INEB – Inst. de Eng. Biomédica, Divisão de Sinal e Imagem, Campus FEUP, 4200-465 Porto, Portugal
[b] ISEP – Inst. Sup. de Eng. do Porto, Dep. de Matemática, Rua Dr. António Bernardino de Almeida 431, 4200-072 Porto, Portugal
[c] FEUP – Faculdade de Eng. da Univ. do Porto, Campus FEUP, 4200-465 Porto, Portugal
[d] Faculdade de Medicina da Univ. do Porto, Dep. de Neurologia, Al. Prof. Hernâni Monteiro, 4200-319 Porto, Portugal
[e] Hospital de São João, Dep. de Neurologia, Al. Prof. Hernâni Monteiro, 4200-319 Porto, Portugal

ARTICLE INFO

Article history:
Received 6 March 2009
Received in revised form 24 July 2009
Accepted 27 September 2009

Keywords:
Ultrasound image
Carotid
Image segmentation
Dynamic programming
Geometric snakes
Thresholding

ABSTRACT

This paper proposes a new approach for the segmentation of both near-end and far-end intima-media regions of the common carotid artery in ultrasound images. The method requires minimal user interaction and is able to segment the near-end wall in arteries with large, hypoechogenic and irregular plaques, issues usually not considered previously due to the increased segmentation difficulty.

The adventitia is detected by searching for the best fit of a cubic spline to edges having features compatible with the adventitia boundary. The algorithm uses a global smoothness constraint and integrates discriminating features of the adventitia to reduce the attraction by other edges. Afterwards, using the information of the adventitia location, the lumen boundary is detected by combining dynamic programming, smooth intensity thresholding surfaces and geometric snakes. Smooth contours that correctly adapt to the intima are produced, even in the presence of deep concavities. Moreover, unlike balloon-based snakes, the propagation force does not depend on gradients and does not require a predefined direction.

An extensive statistical evaluation is computed, using a set of 47 images from 24 different symptomatic patients, including several classes, sizes and shapes of plaques. Bland–Altman plots of the mean intima-media thickness, for manual segmentations of two medical experts, show a high intra-observer and inter-observer agreement, with mean differences close to zero (mean between −0.10 mm and 0.18 mm) and with the large majority of differences within the limits of agreement (standard deviation between 0.10 mm and 0.12 mm). Similar plots reveal a good agreement between the automatic and the manual segmentations (mean between −0.07 mm and 0.11 mm and standard deviation between 0.11 mm and 0.12 mm).

1. Introduction

Atherosclerosis is a disease of blood vessels caused by the formation of plaques in artery walls. Its diagnosis is one of the most important medical examinations for the prevention of cardiovascular events, like myocardial infarction and stroke [1,2].

Plaque echogenicity and texture are classified in categories from I to V, ranging from the homogeneous, uniformly anechogenic (class I) plaque to the homogeneous, uniformly echogenic (class IV) plaque. Mixed forms of plaques are heterogeneous and can be predominantly hypoechogenic (class II) or predominantly echogenic (class III) plaques. Unclassified plaques are considered class V [3].

Atherosclerosis is diagnosed when there are large values of the intima-media thickness (IMT), the distance between the innermost boundaries of the intima and the adventitia of the artery, represented in Fig. 1 as I1 and I3 at the far-end wall. The lumen corresponds to echo zone Z4 and is the region where the blood flows. The media region (echo zone Z2) is delimited by two almost parallel echogenic lines (I2 and I3) separated by a hypoechogenic space, an intensity valley shaped edge known as the 'double line' pattern. The near-end wall has a similar structure, usually with lower definition.

The IMT of extracranial carotid arteries, which can be measured using B-mode ultrasound imaging, provides an index of individual atherosclerosis. Although other measurements of the carotid artery can be used to diagnose atherosclerosis [4,5], the IMT is the most frequently used measure for cardiovascular risk assessment in clinical practice [6]. The bifurcation and the internal carotid artery (ICA) are more prone to atherosclerosis, due to stronger hemodynamic stresses in the bifurcation and branching zones. Unfortunately, it is difficult to visualize the 'double line' pattern at these locations. For these reasons, IMT measurements in the common carotid artery (CCA) have received special attention [7] in the development of segmentation algorithms and in clinical practice.

* Corresponding author. Address: INEB, Divisão de Sinal e Imagem, Campus FEUP, 4200-465 Porto, Portugal. Tel.: +351 966767237; fax: +351 225081624.
E-mail address: rhr@isep.ipp.pt (R. Rocha).

0262-8856/$ - see front matter © 2009 Elsevier B.V. All rights reserved.
doi:10.1016/j.imavis.2009.09.017

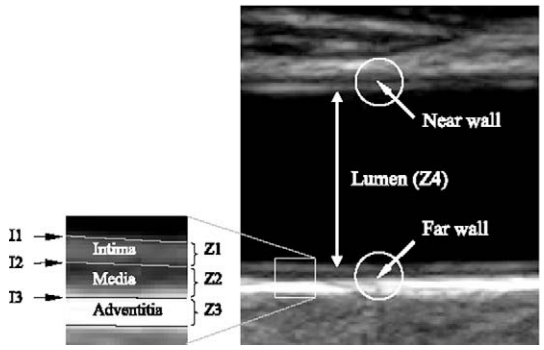

Fig. 1. Intima-media complex in a B-mode image of the common carotid artery (CCA). The lumen (zone Z4) is the region where the blood flows. The CCA wall is formed by the intima (zone Z1), the media (zone Z2) and the adventitia (zone Z3) regions. The boundaries between these four regions are represented by the lines I1, I2 and I3.

The measurement of the IMT is often limited to the far-end wall, due to its better visibility in B-mode images. The segmentation of the near-end wall is also important to applications like the reconstruction of the 3D surface of the artery from 2D B-mode images [8].

Ultrasound imaging has lower cost and smaller risk to the patient than alternative methods like X-ray angiography or intravascular ultrasound [9]. However, B-mode images are a challenge to automatic segmentation due to several degrading factors like [9,10]: speckle [11–14]; echo shadows; movement artifacts; attenuations. The segmentation of diseased arteries brings additional difficulties since there is no shape prior for plaques and the differences between the texture of the plaque and the texture of other nearby tissues are not strong enough for texture-based segmentation [15].

Since the first published attempts to detect the carotid boundaries in ultrasound images [16–18], other more successful techniques have been introduced [19–27]. A summary of the main approaches is given in Table 1, whose structure is similar to the table given in [27] for easier comparison. However, all these techniques have important limitations: (a) large user interaction [16–18,23,27]; (b) consideration of a single image feature [16–18]; (c) performance significantly affected by the presence of large plaques and other boundaries [19,20,22,23,21,25–27]; (d) estimation of optimal weights of a cost function is needed for each boundary [19,20,22]; (e) new training for new equipment settings is required [19,20,22]; (f) do not include global smoothness constraints [19,20,22,23]; (g) contour initialization has to be close to the carotid boundaries [24,21,25,23,27]; (h) gradient-based snakes may leak at boundary gaps and stop at false edges [24,21,25,23,27]; (i) near-end boundaries are not detected [24,21,25–27]. Therefore, the problem of automatic segmentation of the carotid artery in B-mode images remains open and manual segmentation is still a common procedure in clinical practice.

Table 1
Overview of CCA segmentation methods in longitudinal 2D B-mode images.

Methodology	Year	*UI*	*MC*	NE	*LIMT*	*CV*	*N*
DP [19]	1994	Low	No	Yes	No	4.7	44
DP [20]	1997	Low	Yes	Yes	Yes	1.2	69
Multiscale DP [22]	2000	Low	Yes	Yes	Yes	2.0	50
Edge-tracking [23]	2001	High	Yes	Yes	No	–	24
Snakes [25]	2002	Low	Yes	No	Yes	–	32
Gradient based [26]	2005	Low	Yes	No	No	5.4	50
Snakes [27]	2007	High	Yes	No	No	19.1	100

DP: dynamic programming; *UI*: user interaction; *MC*: manual correction allowed; NE: segmentation of the near-end wall; *LIMT*: supports plaques of large IMT (>1.5 mm); *CV*: maximum coefficient of variation (Eq. 7) for the mean IMT in the CCA; *N*: number of subjects.

We introduce a new method for the segmentation of the intima-media region in ultrasound images, which combines splines (for the adventitia detection), dynamic programming (DP), smooth intensity thresholding surfaces [28] and a successful geometric active contour model [29,30] known for its accuracy, flexibility and robustness. Our method presents several attractive features, in particular: it is robust to speckle and irregular contrast; it includes a global smoothness constraint; the initialization of the active contour is automatic; unlike balloon-based snakes, the propagation force of the active contour does not depend on gradients and does not require a predefined direction; several image features are used in the segmentation; no training is required; human interaction is minimal; it is able to segment both near-end and far-end carotid walls; it supports plaques of different sizes, shapes and classes.

Next section describes the materials and methods. It starts by presenting the image data set (Section 2.1) and a description of the manual segmentation (Section 2.2). Section 2.3 gives a brief description of the method used for the detection of the adventitia innermost boundary. A new method for the detection of the lumen boundary, based on dynamic programming, is introduced in Section 2.4. Section 2.5 describes how a hybrid geometric snake and a smooth thresholding surface are used to smooth and improve the location of the lumen boundaries detected by the DP algorithm. The parameter settings are discussed in Section 2.6. Section 2.7 presents the evaluation methodologies. Results are shown in Section 3 and discussed in Section 4. Finally, some conclusions and topics for future work are given in Section 5.

2. Materials and methods

2.1. The image dataset

A set of 47 longitudinal B-mode images of the CCA was acquired with a Philips HDI 5000 ultrasound system and recorded with 256 gray levels. The resolution was normalized to 0.09 mm, a common value used in clinical practice.

The image set was taken from 24 different symptomatic patients, with several classes (classes II–IV), sizes and shapes of plaques. An image was selected if the medical doctor was able to make at least a rough outline of the intima-media region boundaries, in the B-mode image, without any complementary information like power-Doppler imaging. The sample includes cases with boundary gaps, where the location of the boundary had to be inferred.

2.2. Manual segmentation

All images were manually segmented by two medical experts, A and B, and twice by one of the experts (A), at two moments separated by a period of one year. The manual segmentations consisted in the delineation of the innermost boundaries of the adventitia and the intima, at the near-end and far-end carotid walls. They were performed using software developed in Matlab and saved for later comparison between each other and with the automatic segmentation.

Hereafter, the manual segmentations of expert A and expert B and the automatic segmentations will be referred to as MA1, MA2, MB1 and A, respectively.

2.3. Detection of the carotid adventitia

The approach proposed in [8] is used to automatically detect the carotid adventitia. The geometry of the adventitia contour is mod-

eled by a cubic spline with five control points. The method looks for the best smooth path in longitudinal B-mode images, according to the following gain function:

$$G = \frac{1}{2m}\sum_{k=1}^{m}[g_1(P_k) + g_2(P_k)]g_3(P_k)g_4(P_k) \quad (1)$$

where m is the number of P_k points of the digital spline and $g_j(P_k),\ 1 \leqslant j \leqslant 4$, is a fuzzy function representing the contribution of feature j at point P_k. This function integrates four different discriminating features: the proximity of the geometric model to any edge (g_1) or to valley shaped edge (g_2) pixels; the consistency between the orientation of the normal to the geometric model and the intensity gradient (g_3); and the distance to a rough estimate of the lumen boundary (g_4).

The search for the best fit of the cubic spline is implemented in an efficient way through a random sample consensus (RANSAC) algorithm [31]. This algorithm allows the estimation of model parameters from a data set containing a large number of outliers. It works by repeatedly extracting a random sample from the data set, with the minimum sample size required to determine the model parameters. The consensus of the model is then evaluated on the remaining population and the model with the best consensus is selected. In our case, the consensus is measured by Eq. (1).

The approach starts by estimating the lumen medial axis from two or three points specified by the user. The estimated lumen axis is used to determine a rectangular region of interest (ROI). It is also used, together with the triangle thresholding algorithm [32], to obtain a rough estimate of the lumen region.

An edge map is computed using a new smoothing filter [8], nonmaxima suppression and hysteresis thresholding [33]. The smoothing filter borrows concepts from robust statistics and the total variation theory [34,35], showing an improved detection of important edges when compared to previously published filters. It also integrates an edge detector well adapted to ultrasound images, known as the instantaneous coefficient of variation (ICOV) [11,12]. The ICOV value at pixel (x,y) is given by:

$$\mathrm{ICOV}(x,y) = \sqrt{\frac{\left|\frac{1}{2}\|\nabla I(x,y)\|^2 - \frac{1}{16}(\nabla^2 I(x,y))^2\right|}{\left(I(x,y) + \frac{1}{4}\nabla^2 I(x,y)\right)^2}} \quad (2)$$

where $I(x,y)$ represents the image intensity at (x,y), $\nabla I(x,y)$ is the intensity gradient at (x,y), $\|\nabla I(x,y)\|^2 = 0.5[\|\nabla_- I(x,y)\|^2 + \|\nabla_+ I(x,y)\|^2]$, $\nabla_- I(x,y) = (I(x,y) - I(x-1,y), I(x,y) - I(x,y-1))$, $\nabla_+ I(x,y) = (I(x+1,y) - I(x,y), I(x,y+1) - I(x,y))$, $\nabla^2 I(x,y) = I(x+1,y) + I(x-1,y) + I(x,y+1) + I(x,y-1) - 4I(x,y)$ and $\|(u,v)\| = \sqrt{u^2+v^2}$ is the norm of a vector (u,v).

Intensity gradient orientation errors are reduced by computing the local dominant gradient direction.

To reduce the computational cost, edges that are incompatible with the adventitia contours are removed before the RANSAC search begins. An edge pixel is considered incompatible if the angle between its local dominant gradient and the gradient of the distance map to the medial axis is too large (at least 30°). Edges whose distance to the estimated lumen medial axis is too large (more than 8 mm) are also removed.

Statistical analysis and some examples of the adventitia detection are presented in Section 3.

2.4. Estimation of the lumen boundary using DP

The location of the lumen boundary is essential for the determination of the IMT. However, hypoechogenic plaques may be very difficult to detect, except for a thin and discontinuous path along the boundary between the plaque and the lumen. Therefore, the method proposed for the detection of the lumen boundary uses DP to search for the best path. It assumes the carotid adventitia was previously detected (using the approach described in Section 2.3) and can be summarized as follows:

(1) Set $E_{\mathrm{all}}(x,y) = 1$ if (x,y) is a local maximum of the ICOV in the direction of $\nabla I(x,y)$. Otherwise, $E_{\mathrm{all}}(x,y) = 0$. E_{all} is the edge map with all edges (Fig. 2b), obtained as described in Section 2.3 but without any constraint on the edge strength, measured by the ICOV. This edge map is important because some edges of the lumen boundary may be quite weak.
(2) Set $E_{\mathrm{strong}}(x,y) = E_{\mathrm{all}}(x,y)$ if $\mathrm{ICOV}(x,y) > T$, where T is a threshold automatically estimated with robust statistics [8]. Otherwise, set $E_{\mathrm{strong}}(x,y) = 0$. E_{strong} is the edge map with the strong edges (Fig. 2c).
(3) Set $E(x,y) = E_{\mathrm{all}}(x,y)$ if $(x,y) \in \Omega$, where Ω is the inner region delimited by the detected adventitia contours. Otherwise, $E(x,y) = 0$.
(4) Set $E(x,y) = 0$ and $E_{\mathrm{strong}}(x,y) = 0$ if $\gamma(x,y) \geqslant 90°$, where γ is the angle between $\nabla I(x,y)$ and $\nabla D(x,y)$ and D is the distance map to the lumen medial axis (Section 2.3). This step removes the edges of E and E_{strong} that have a gradient pointing inwards the artery, which means they are incompatible with the intima. Fig. 2d illustrates the result of this step for E_{strong}.
(5) If $E(x,y) = 1$, compute $\mathrm{ICOV}^*(x,y) = \mathrm{ICOV}(x,y)/\max_y(\mathrm{ICOV}(x,y))$, the normalized ICOV at (x,y) in the vertical direction. ICOV^* is computed separately for edges above and below the lumen axis, for each abscissa. This procedure gives a chance to the usually weaker lumen boundary edges to compete with the adventitia edges. Otherwise, the DP contour tends to be attracted toward the adventitia, where the ICOV is much stronger.
(6) Set $E(x,y) = 1$ if $E_{\mathrm{strong}}(x,y) = 1$ and there are no other edges in E_{strong} between (x,y) and the lumen axis, in the vertical direction (Fig. 2e and f). This is required because the carotid adventitia is the best estimate of the lumen boundary when the intima-media region is not visible. Set $\mathrm{ICOV}^*(x,y) = 1$ for these edges.
(7) Using DP, look for the path in E, between the first and the last columns of the ROI, that minimizes the cost function

$$C_t = \sum_{j=1}^{N}\psi(x_j,y_j) \quad (3)$$

where $\psi(x_j,y_j) = 1 - \mathrm{ICOV}^*(x_j,y_j)$ if $E(x_j,y_j) = 1$ and $\psi(x_j,y_j) = 1$ otherwise; N is the number of columns of the ROI.

In longitudinal sections of the carotid, there are two intima contours, one above and the other below the lumen medial axis. Both contours start at the first column and finish at the last column of the edge map E. Therefore, the DP algorithm can be applied directly to E, with independent searches made above and below the lumen axis. Fig. 3 shows the lumen boundaries detected by the proposed DP algorithm in two different images.

A geometric term could have been included in Eq. (3) in order to smooth the estimated contours. This was not done because a strong geometric term would often be necessary to overcome strong values of the ICOV at undesired edges, leading to bypasses of the contour through tissue regions at sections of the lumen boundary with high curvature caused by plaque formation. Besides, the roughness of the detected contours can easily be eliminated through an independent smoothing using a geometric snake, as described in the next subsection.

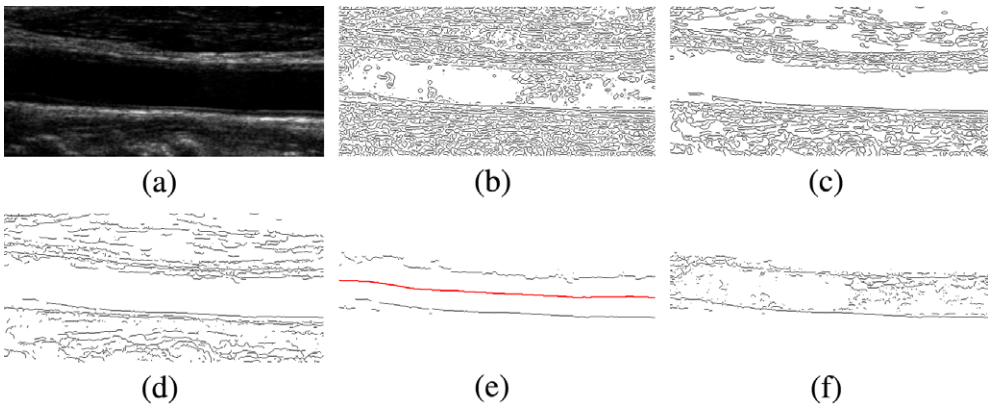

Fig. 2. (a) ROI from a B-mode image of a longitudinal section; (b) edge map E_{all}, with all edges (strong and weak); (c) edge map E_{strong}, containing only strong edges; (d) E_{strong} after removing all edges with a gradient direction incompatible with the intima; (e) edges of E_{strong} that are 'visible' from the interpolated lumen axis (red curve); (f) final version of edge map E.

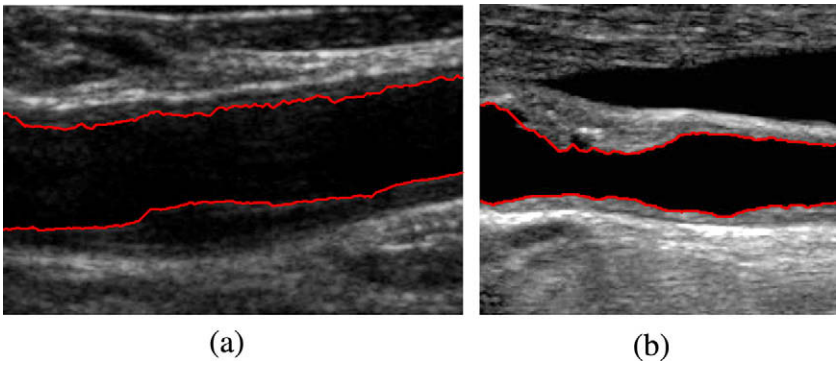

Fig. 3. Lumen boundaries detected with DP in two different images.

2.5. Smoothing and improving the detected lumen boundaries

The output of the DP algorithm often has irregularities caused by noise or defective detections of the carotid boundaries. Moreover, the DP approach cannot correctly detect deep concavities nor sharp saliences, as the one in the left part of the upper lumen boundary in Fig. 3b. However, it is possible to significantly reduce these location errors through a region-based active contour, which also produces smoother curves. For this purpose, we introduce a hybrid version of the Chan–Vese piecewise constant segmentation model [29,30] that is better suited to B-mode ultrasound images.

The Chan–Vese geometric snake is a successful active contour due to its potential, flexibility and accuracy. It is a region-based model embedded in a level set framework [36,37] that does not depend on gradients, which makes it robust to the initial position of the active contour and to small gaps in the boundaries. Moreover, it has the ability to automatically detect inner contours, its topological changes are treated in a natural way and the direction of its evolution in space is automatically determined from the image data.

The Chan–Vese active contour is a particular case of the more general image segmentation variational model of Mumford and Shah [38]. It assumes a two-phase piecewise constant image and is described by the functional

$$F(c_1,c_2,C) = \mu\cdot\text{Length}(C) + \lambda_1\int_{inside(C)}[u_0(x,y)-c_1]^2dxdy + \lambda_2\int_{outside(C)}[u_0(x,y)-c_2]^2dxdy \quad (4)$$

where μ, λ_1 and λ_2 are positive parameters, $u_0:\Omega\to\mathbb{R}$ represents the input image, c_1 and c_2 are, respectively, the averages of u_0 inside and outside the region boundaries represented by C. In [29], a level set formulation was introduced for Eq. (4), where the active contour, C, is represented as the zero level set of an implicit function.

The major difficulty in the application of this active contour to B-mode images of the carotid is their non-piecewise constant nature. However, this problem can be solved by introducing some modifications to the Chan–Vese model.[1]

In the Chan–Vese model, the values of c_1 and c_2 are estimated, in each iteration, by minimizing the mean square distance between the gray-scale image and the binary image produced by the segmentation. Therefore, c_1 and c_2 can be viewed as functions of an intensity threshold that is updated as the active contour evolves in space.

We propose a hybrid Chan–Vese active contour that is not only faster than the original model but also better suited for piecewise smooth images. The intensity threshold estimate of the Chan–Vese model is replaced by a thresholding surface, keeping the other attractive properties. Basically, this algorithm consists of two stages:

(1) An optimal smooth thresholding surface, $T_{opt}(x,y)$, is interpolated from the intensities at the edges along the boundaries produced by the DP algorithm. This is done only once, before the initialization of the active contour.
(2) The image is then processed by a modified version of the

[1] There is a piecewise smooth version of the Chan–Vese active contour [30] but it proved to be of little utility in this type of images due to its computational complexity and its tendency to stop at local minima of the functional.

Chan–Vese two-phase piecewise constant active contour, where c_1 and c_2 are determined as functions of $T_{opt}(x,y)$, such that the intensity threshold at each pixel is given by the thresholding surface.

In the hybrid model, we set $c_1(x,y) = 2T_{opt}(x,y)$ and $c_2(x,y) = 0$, to keep the intensity threshold as the mean of c_1 and c_2. Unlike the Chan–Vese model, the active contour is not used to estimate the intensity threshold since the values of c_1 and c_2 in Eq. (4) are not updated during the evolution of the contour. The active contour is used only to smooth and to improve the position accuracy of the estimated boundaries.

2.5.1. Thresholding surface

Inspired by the Yanowitz' algorithm [28], a new method was devised to estimate the thresholding surface, $T_{opt}(x,y)$, by interpolating the image intensities at edge pixels, where good local thresholds are expected to be found. The interpolation surface is obtained by solving the Laplace's equation

$$\frac{\partial^2 u}{\partial x^2} + \frac{\partial^2 u}{\partial y^2} = 0 \tag{5}$$

for the thresholding surface, u.

Eq. (5) is computed in two steps. First, an approximate solution is obtained with a fast algorithm that propagates the intensity values at the interpolating pixels to the rest of the image. Second, the Laplace's equation is solved with the following numerical scheme:

$$\begin{aligned} u^{n+1}(x,y) &= 0.25[u^n(x+1,y) + u^n(x-1,y) + u^n(x,y+1) + u^n(x,y-1)] \\ u^{n+1}(x,y) &= \beta u^{n+1}(x,y) + (1-\beta)u^n(x,y), \quad n = 0,1,2,\ldots \end{aligned} \tag{6}$$

where $u^n(x,y)$ is the value of the thresholding surface at pixel (x,y) and at iteration n, $\beta = 1.5$ and the initial solution, u^0, is the surface in the first step.

The second equality in Eq. (6) introduces over-relaxation [39] to speed up the convergence. The iterations are stopped when the relative intensity difference for every pixel is less than 1% between two consecutive iterations.

In the intensity propagation step, the Euclidean distance map to the interpolating pixels is computed with a fast algorithm [40]. Then, the other pixels are ordered in a list by ascending value of the computed distance and processed in that order. At each pixel in the list, the intensity threshold is computed as a weighted average of the thresholds found for its 8-neighbors with smaller distance to the interpolating pixels. The weights are inversely proportional to the distances of the central pixel to the selected neighbors. This solution is not very smooth but it can be computed quickly, reducing the total computational effort when used to initialize the numerical scheme for the Laplace's equation.

2.5.2. Important details of the active contour

The implicit function of the hybrid Chan–Vese model is initialized as a signed distance function for which the zero level sets are the curves produced by the DP algorithm. Since these curves are already close to the real lumen boundaries, the number of iterations is reduced.

To further reduce the computational effort, the processing is limited to the smallest rectangular box containing both adventitia contours.

The Chan–Vese model spontaneously detects the interior of objects in an image, as the holes illustrated in Fig. 4b. While this is desirable in most cases, it should be avoided in our case so that other independent dark regions are not classified as lumen. The detection of new regions is avoided if the implicit function becomes unable to generate new isolated zero level sets. A fast and simple way to achieve this goal is to inhibit a sign change in the implicit function at any pixel for which there is no 8-neighbor with the same new sign. In other words, the implicit function is allowed to change sign only at pixels in the vicinity of the active contour. An example of the effect introduced by this constraint is presented in Fig. 4c.

Since the adventitia is detected before the intima, the evolution of the active contour is constrained to the region delimited by the adventitia, inhibiting any contour leakage at wall sections with weak echo or no echo at all. This constraint is implemented by setting the intensities of the pixels outside the carotid to the highest value of the image gray scale. Fig. 4 shows an example of a contour leakage, through the carotid wall, which is stopped by this constraint.

In some cases, the active contour may also leak through the lumen boundary produced by the DP algorithm, at places where boundary edges are missing. One way to reduce this risk is to compute the thresholding surface under the constraint that it drops to zero at some reasonable distance, d, from the carotid. This results in lower values of the thresholding surface outside the detected lumen boundary. Other possibilities are: (i) to apply a smoothing filter to the intensity profile along the contour produced by the DP algorithm and (ii) to propagate the smallest of the intensities at consecutive edges of the DP contour to the pixels along the contour that are between those edges. In practice, the first solution gave the best results. To keep some safety margin from the carotid wall, d was set to $3\sigma_d$, where $\sigma_d = 4$ pixels is a parameter used in the algorithm described in Section 2.3 [8] and defined as the maximum expected distance between a carotid adventitia edge and the fitted spline. Fig. 5 shows the thresholding surfaces with and without the additional constraint, for the image presented in Fig. 4.

Two examples of the final contour are presented in Fig. 6. The second example shows the significant improvement in the location of the left part of the upper lumen boundary, capturing the plaque concavities that could not be detected by the DP algorithm alone (see also Fig. 3). In both cases, the ground truth is also displayed.

2.6. Parameter settings

There are several parameters to be defined in the Chan–Vese two-phase piecewise constant active contour. With the exception of parameter μ, which determines the elastic strength of the contour, all the others were set as suggested in [29,30]. Equal importance is given to both phases in the image by choosing $\lambda_1 = \lambda_2 = 1$. Eq. (4) was solved with the semi-implicit numerical scheme proposed in [29,30], using a time step $\Delta t = 0.1\Delta x$ and set-

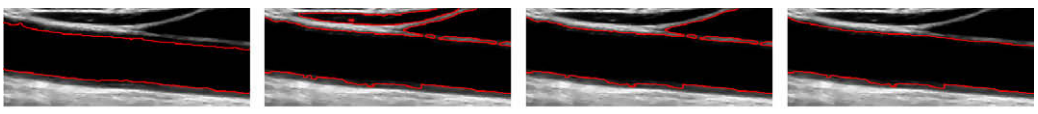

Fig. 4. Inhibiting the detection of new holes and leakages in the Chan–Vese model: (a) initial active contour; (b) segmentation result without inhibiting the detection of new holes or leakages; (c) result when the detection of new holes is inhibited; (d) result constraining the evolution of the active contour to the region inside the carotid adventitia contour.

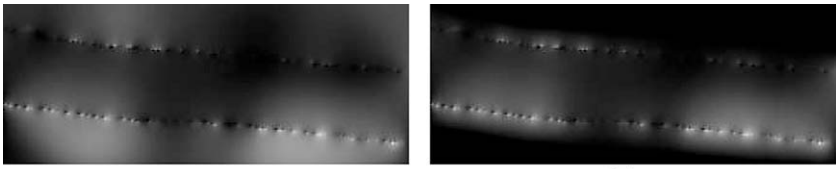

Fig. 5. Thresholding surfaces computed for the image of Fig. 4: (a) without the constraint of dropping to zero at distance $3\sigma_d$ from the carotid and (b) with the referred constraint.

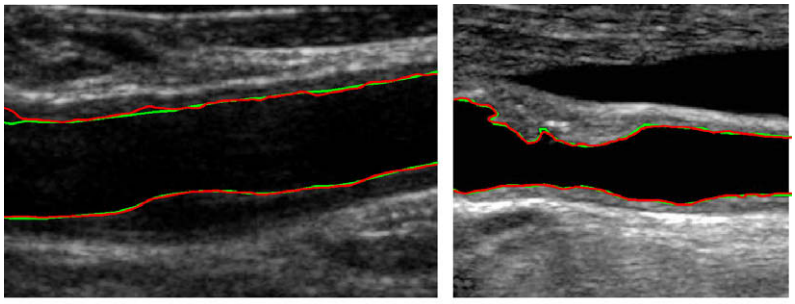

Fig. 6. Ground truth (green) and the lumen boundaries obtained with the hybrid Chan–Vese model (red) from the contours displayed in Fig. 3.

ting $\Delta x = \Delta y = 1$, where $(\Delta x, \Delta y)$ represents the image grid size. This numerical scheme was iterated until the maximum distance covered by the active contour became less than $0.01\Delta x$, between two consecutive iterations. In other words, iterations were terminated when the active contour evolution virtually stopped.

Parameter μ can also be seen as a scale parameter, in the sense that the size of the smallest objects detected by the active contour is proportional to the value of μ. Therefore, this parameter was defined as a function of the scale of the segmented lumen, measured by the length, L, of the lumen boundary produced by the DP algorithm. In longitudinal sections, L is the perimeter of the region delimited by the two estimated contours (one above and the other below the medial axis). The scale parameter was set as $\mu = \rho L \times 255^2$, where $\rho = 10^{-4}$ was empirically determined as a compromise between a satisfactory level of smoothing and the fidelity to the data. The factor 255^2, also used in [29,30], is necessary to keep unity consistence in the level set equation, since the image intensities are represented in the range $\{0,\ldots,255\}$.

2.7. Evaluation methodology

Several statistics and statistical analysis were used to evaluate the results. In each image, their computation was based on the vertical distance between contours at every abscissa that is common to manual and automatic contours.

Some of the statistics are: (a) $D_{\max}$, the maximum vertical distance between corresponding contours obtained from two different segmentations, e.g., between the automatic contour (A) and a homologous manual contour; (b) D_{mean}, the mean vertical distance between homologous contours obtained from two different segmentations; (c) $\text{IMT}_{\min}$, IMT_{mean} and $\text{IMT}_{\max}$, the minimum, mean and maximum IMT of each segmented intima-media region, respectively.

To estimate the inter-method (manual versus automatic), the intra-observer and the inter-observer errors, defined as $se = sd/\sqrt{2}$ [19], two other statistics were computed: the pooled mean, $\bar{x}$, and the standard deviation, sd, of the differences in $\text{IMT}_{\min}$, IMT_{mean} and $\text{IMT}_{\max}$ measures between two given manual segmentations or between a manual segmentation and the automatic one. The coefficient of variation, CV, for $\text{IMT}_{\min}$, IMT_{mean} and $\text{IMT}_{\max}$ was also computed, as [19]

$$CV = 100\frac{se}{\bar{x}}\% \tag{7}$$

Box plots, linear regression analysis and Bland–Altman plots [41] were used to assess the agreement between methods and between observers.

3. Results

3.1. Segmentation examples

Some examples of good and defective automatic detections of the lumen boundary are presented in Figs. 7 and 8, respectively, along with the corresponding MA1 segmentations, for comparison.

Figs. 9 and 10 show examples of the intima-media region and the corresponding boundaries automatically detected, using the proposed algorithm for the lumen boundaries and the algorithm described in Section 2.3 for the carotid adventitia.

3.2. Statistical analysis

An automatic detection of a boundary was considered to be successful if $D_{\max} < 1$ mm between the automatic contour and any of the corresponding manual versions. In the tested set of 47 B-mode images of the CCA, 81 out of the 94 adventitia boundaries were successfully detected, giving a success rate of 86.2%. Fig. 11 shows the distribution of the $D_{\max}$ statistic for the subset of adventitia contours with $D_{\max} < 1$ mm.

Since the automatic detection of the intima depends on the location of the automatically detected adventitia, the $D_{\max}$ and D_{mean} statistics for the intima were computed only for the subset of 81 intima-media complexes with successful detection of the adventitia. Successful detections of the intima boundary were obtained in 66 out of the referred 81 intima-media complexes, corresponding to a success rate of 81.5%. The distribution of $D_{\max}$ and

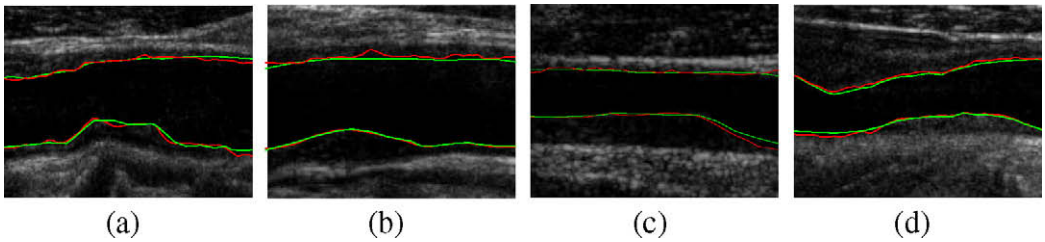

Fig. 7. Examples of good automatic detections of the lumen boundaries (red curves) along with the corresponding MA1 segmentations (green curves).

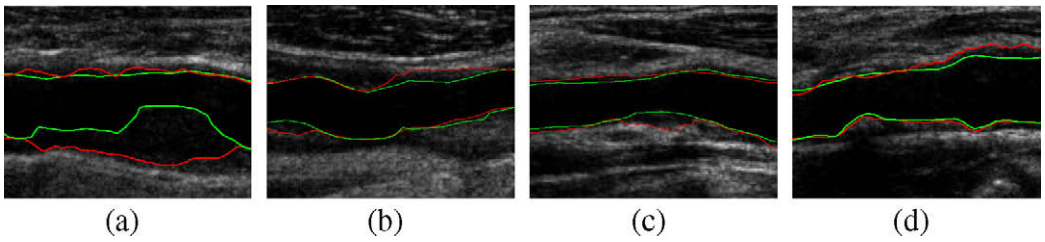

Fig. 8. Examples of defective automatic detections of the lumen boundaries (red curves) along with the corresponding MA1 segmentations (green curves).

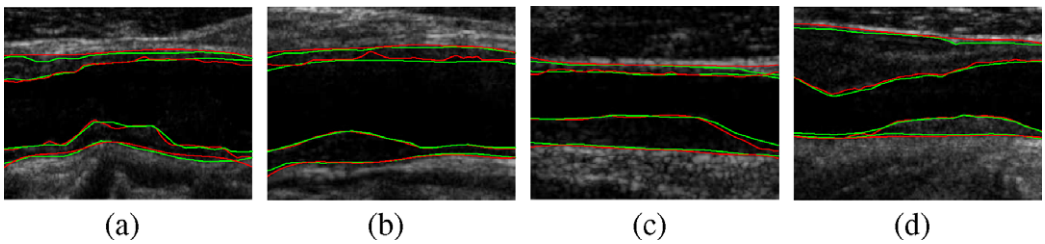

Fig. 9. Automatic detections (red curves) of the intima-media boundaries, along with the corresponding manual (MA1) segmentations (green curves).

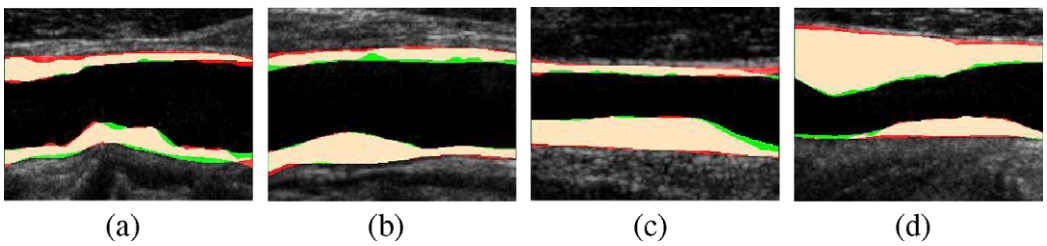

Fig. 10. Automatic and manual segmentations of the intima-media regions: green areas – only detected in the manual segmentation (MA1); red areas – only detected in the automatic segmentation; beige areas – detected by the manual and the automatic segmentation.

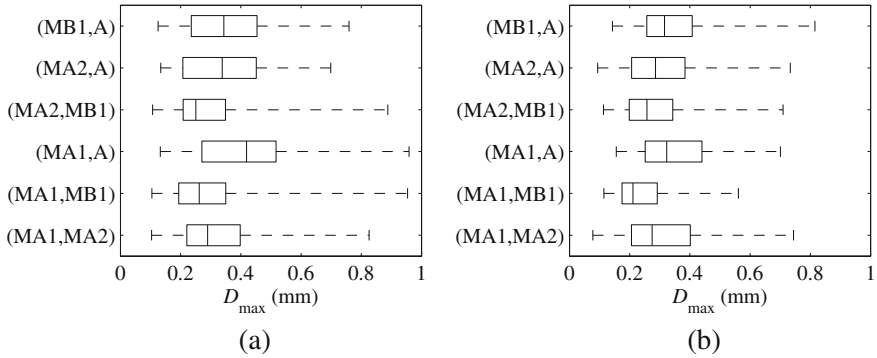

Fig. 11. D_{max} statistics for the adventitia detections with $D_{max} < 1$ mm: (a) near-end boundary and (b) far-end boundary.

D_{mean} for the intima detections with $D_{max} < 1$ mm can be found in Figs. 12 and 13.

The rest of the statistical analysis presented in this section evaluates the intra-observer, inter-observer and inter-method errors, the correlation strength with varying IMT and the degree of agreement between the methods. This evaluation is computed only for the 66 intima boundaries successfully detected by the automatic method.

Table 2 shows the inter-method (manual versus automatic), the intra-observer and the inter-observer errors, as well as the coefficient of variation, *CV*, for IMT_{min}, IMT_{mean} and IMT_{max}, defined in Section 2.7.

Fig. 14 shows the correlation coefficient, *r*, the regression lines and the corresponding equations, $y(x)$, for the mean IMT, showing very high correlation coefficients ($0.973 \leqslant r \leqslant 0.978$) between the automatic segmentations and the manual ones. Moreover, these values are similar to those obtained when comparing different manual segmentations ($0.977 \leqslant r \leqslant 0.981$) and all regression lines are close to the line of equality.

Fig. 15 shows the Bland–Altman plots of the differences between the mean IMT of two given segmentations against their average. The standard deviation is represented by SD and the limits of agreement, in the form mean $\pm$ 2SD mm, are: 0.03 ± 0.22 between MB1 and A, -0.07 ± 0.24 between MA2 and A, -0.10 ± 0.20 between MA2 and MB1, 0.11 ± 0.24 between MA1 and A, 0.08 ± 0.24 between MA1 and MB1, 0.18 ± 0.24 between MA1 and MA2.

The estimated median computing time is 0.0470 s for the DP algorithm, 18.5 s for the Chan–Vese algorithm and 18.9 s for the whole intima segmentation procedure. The median computing time required to segment the adventitia is 28.5 s. The computations were done using Matlab on a computer equipped with an Intel Core 2 Duo processor at 2.13 GHz.

Table 2
Comparison between manual and automatic measures of the IMT at near-end (NE) and far-end (FE) boundaries.

		IMT_{min}		IMT_{mean}		IMT_{max}	
		se	*CV*	*se*	*CV*	*se*	*CV*
(MB1,A)	NE	0.15	21.3	0.09	8.7	0.13	9.0
	FE	0.13	25.0	0.08	7.7	0.16	10.3
(MA2,A)	NE	0.12	16.9	0.09	8.6	0.13	9.1
	FE	0.12	21.9	0.09	8.4	0.15	9.3
(MA2,MB1)	NE	0.08	10.2	0.08	7.4	0.14	9.7
	FE	0.09	15.4	0.07	6.9	0.11	6.9
(MA1,A)	NE	0.11	18.0	0.09	9.1	0.12	8.7
	FE	0.13	26.7	0.08	8.3	0.15	9.9
(MA1,MB1)	NE	0.10	15.5	0.10	10.9	0.13	10.0
	FE	0.10	18.4	0.06	6.5	0.09	6.2
(MA1,MA2)	NE	0.09	12.2	0.09	8.7	0.12	9.0
	FE	0.11	18.7	0.07	7.2	0.11	7.0

se: in ter-observer, intra-observer and inter-method error in mm; *CV*: coefficient of variation in percentage (Eq. (7)).

4. Discussion

The main purpose of this work was the development of a robust method that is able to segment the carotid walls in B-mode images of the CCA, even in the presence of plaques of different sizes, shapes and classes. It should be able to segment not only the far-end wall but also the near-end wall in arteries with large, hypoechogenic and irregular plaques, situations not addressed previously due to the increased segmentation difficulty. It should also require minimal user interaction and independence of equipment settings. Therefore, manual corrections of computer generated contours were not considered, although they could be easily introduced to further improve the results. A slightly larger dispersion of the automatic measures was observed when compared to manual

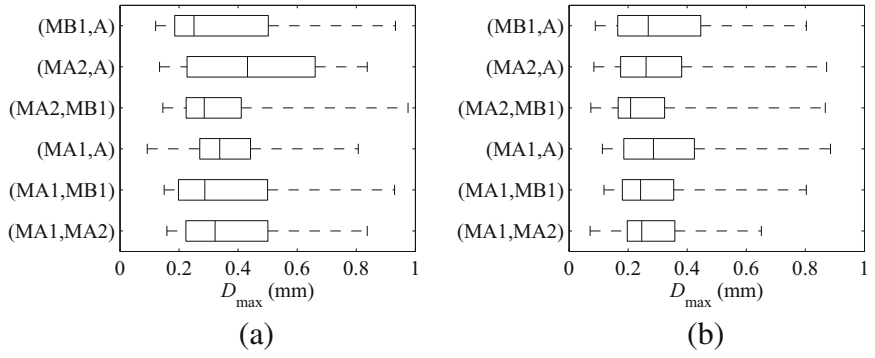

Fig. 12. D_{max} statistics for the intima detections with $D_{max} < 1$ mm: (a) near-end boundary and (b) far-end boundary.

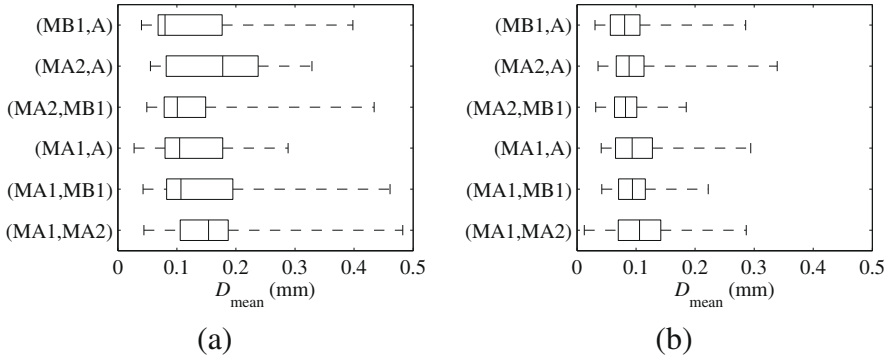

Fig. 13. D_{mean} statistics for the intima detections with $D_{max} < 1$ mm: (a) near-end boundary and (b) far-end boundary.

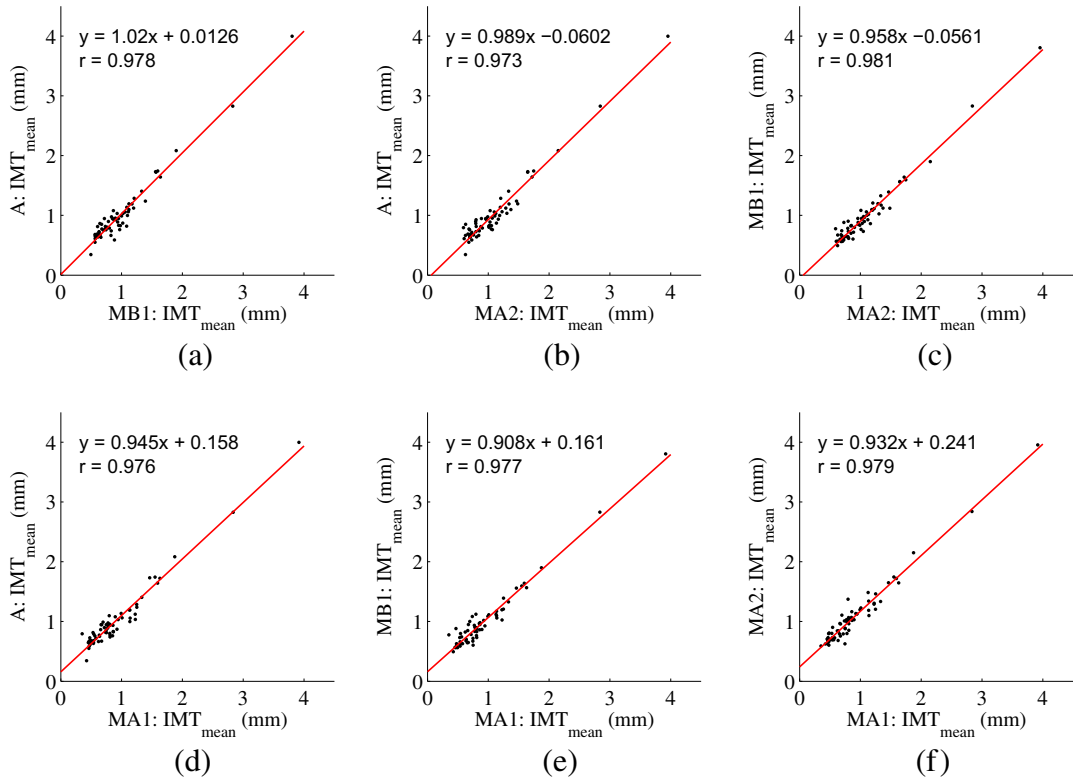

Fig. 14. Regression analysis of the mean IMT for the automatic and the manual segmentations.

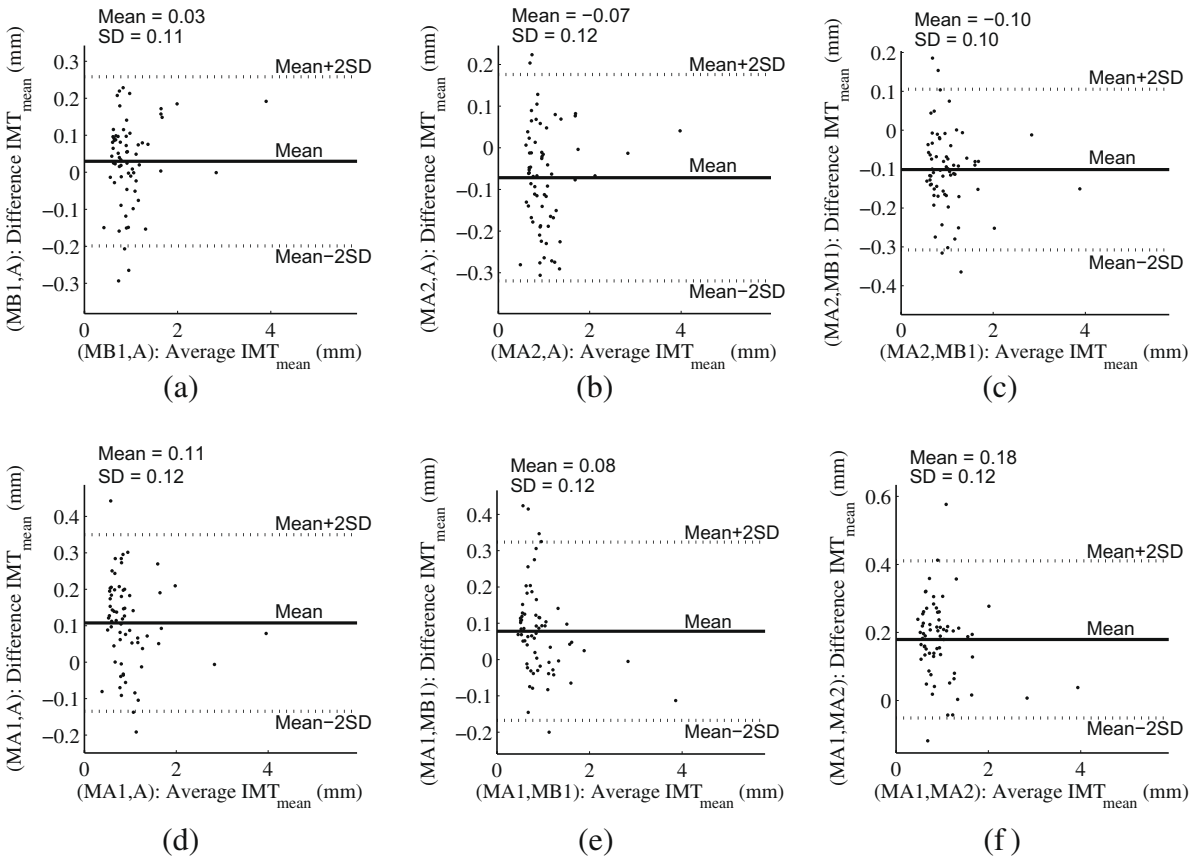

Fig. 15. Bland–Altman plots of the mean IMT for the automatic and the manual segmentations, where SD represents the standard deviation.

ones, specially for images of poor quality and for near-end walls. However, as discussed below, the statistical analysis showed promising results.

For the adventitia, the distribution of D_{max} (Fig. 11) leads to three main observations. First, the values of D_{max} and their variability are larger for near-end boundaries, which is in agreement with the lower visibility of these boundaries and the greater difficulty of their detection by both the medical experts and the computer. Second, D_{max} tends to be higher when one of the compared contours is automatic, although the difference is small in general and very small for far-end boundaries. In at least 75% of the near-end cases, $D_{max} < 0.4$ mm when comparing two manual adventitia contours while $D_{max} < 0.51$ mm when one of the compared contours is automatic. Considering the same percentile for the far-end adventitia boundaries, $D_{max} < 0.40$ mm for pairs of manual contours and $D_{max} < 0.43$ mm for the other pairs. Third, some automatic detections are too far away from the manual versions. In some of these cases, the distances between different manual contours are also high, probably due to a poor quality of the images. However, there are false automatic detections of the adventitia boundaries in 13.8% of the cases.

For the intima, the detection results (Figs. 12 and 13) are also worse at the near-end intima boundary than at the far-end one. The larger values of D_{max} for the intima, when compared to the adventitia, are a consequence of the poorer visibility of the intima boundaries. In fact, the intima region is often much darker and has less contrast than the adventitia, leading to a larger uncertainty in the intima location. This also explains why the percentage of false automatic detections is higher for the intima (18.5%) than for the adventitia.

Analyzing D_{max} and D_{mean} by quartiles, the intima automatic detection is quite good within the lower quartile ($D_{max} < 0.27$ mm and $D_{mean} < 0.08$ mm), due to the well defined contours, while the results in the upper quartile reflect a worse accuracy ($D_{max} < 0.94$ mm and $D_{mean} < 0.4$ mm) caused by a greater ambiguity of the contour location.

The larger variability for IMT_{min} (values of *se* and *CV* in Table 2) than for IMT_{mean} and IMT_{max} can be explained by the poor definition of the intima boundaries at some very thin intima-media regions. The corresponding inter-method variability is higher because, when there are gaps in intima boundaries close to the adventitia, the expert can infer the correct location of the intima while the automatic procedure just looks for the closest compatible edges. Compared to IMT_{min}, the inter-method variability for IMT_{mean} and IMT_{max} is more important to the diagnosis of atherosclerosis and it is only slightly larger than the homologous variability of manual segmentations.

The regression analysis for the mean IMT, presented in Fig. 14, shows correlation coefficients between the automatic and the manual segmentations ($0.973 \leqslant r \leqslant 0.978$) similar to the ones obtained between manual segmentations ($0.977 \leqslant r \leqslant 0.981$). The automatic segmentation of large plaques presents a good correlation with the corresponding manual segmentations, in spite of the errors introduced by hypoechogenic plaques. All regression lines are very close to the line of equality, which means a strong agreement between the methods.

The Bland–Altman plots of the mean IMT (Fig. 15) for manual segmentations show a high intra-observer and inter-observer agreement, with mean differences close to zero (-0.10 mm $\leqslant$ mean $\leqslant 0.18$ mm), small values of the standard deviation (0.10 mm $\leqslant$ SD $\leqslant 0.12$ mm) and almost all differences within the limits of agreement ($[\text{mean} - 2\text{SD}, \text{mean} + 2\text{SD}]$). The plots indicate a good agreement between the automatic and the manual segmentations, with similar values of the mean differences (-0.07 mm $\leqslant$ mean $\leqslant 0.11$ mm) and of the standard deviation (0.11 mm $\leqslant$ SD $\leqslant 0.12$ mm).

Although better results have been reported by others (e.g. [19]), the direct comparison to previously published results is not easy and can be misleading for three reasons. First, the image set is not the same and the larger inter-observer and intra-observer errors obtained in our statistical analysis suggest a poor quality of the images. Second, as discussed below, most of the other works have more limited application scope. Third, no manual correction was applied in the present study.

In the DP approach introduced in [19,20], the automatic measurements presented a smaller variability than the manual ones, with $CV \leqslant 4.7$ and $r \geqslant 0.95$ for IMT_{mean}. However, it is not clear what was the treatment given to segmentation errors in [19] while in [20] the results were influenced by the manual correction of these errors. In both cases, a training procedure is required, making the method dependent on the equipment settings. The same comments are applicable to [22], where $CV \leqslant 2.0$ and $r = 1.00$ for IMT_{mean}. The basic idea behind this method is similar to [19,20], although with some improvements like a multiscale approach and the integration of the manual corrections in the DP cost function.

Large user interaction is required in the edge-tracking method in [23], in order to initialize the contour near the boundary. Only healthy subjects were considered in the study, which means that cases with plaques were not included. The results were influenced by manual corrections of the segmentation errors and the IMT was measured only at the far-end wall. The computer generated contours were not compared to manual detections.

The gradient-based snake presented in [25] was tested only at the far-end wall. The adventitia is detected after the intima, displacing the snake downward about 0.05 cm. Therefore, it will probably fail to correctly detect the adventitia in images with large plaques since, in these cases, there is a large chance of finding other edges above the adventitia. No values were given for the coefficient of variation or the coefficient of correlation.

In [26], $CV \leqslant 5.4$ and $r \geqslant 0.915$ were obtained for IMT_{mean} but only the far-end wall and small IMT values (IMT < 1.2 mm) were considered. Initial user interaction is reduced, consisting in one mouse click in the lumen at the left limit of the arterial region to be segmented. The automatic segmentation is based on image gradient and intensity information but very few details of the method are given. Therefore, it is difficult to evaluate how it would behave in the presence of large plaques. Moreover, the results were influenced by manual corrections.

Some important findings were reported in [27,42], like the improvement on results caused by image normalization and speckle reduction. The results for IMT_{mean} showed that $CV \leqslant 19.1$ while a mean of -0.01 and a standard deviation of 0.12 were obtained in the Bland–Altman plots. However, the image normalization is performed manually. The method was not applied to near-end walls. After the detection of the adventitia, the snake is displaced up to 1.02 mm upwards, to detect the intima. On the other hand, the snake is based on gradients and can be trapped by erroneous edges. Therefore, it has to be initialized as close as possible to the boundary to be detected and it cannot be used in cases where the IMT is larger than 1.4 mm, leaving out atherosclerotic plaques. Finally, the results are influenced by manual corrections.

Our approach is based on DP. However, an intrinsic limitation of the DP approach is its inability to capture deep concavities and sharp saliences. Another limitation is the difficulty in integrating global smoothing constraints, which could help improving the poor response at very degraded parts of the lumen boundary. An alternative way to introduce some smoothing is to integrate a geometric term in the cost function, but this solution may cause undesirable bypasses through the interior of tissue regions. The results showed that an independent geometric snake can produce the desired smoothing and also capture deep concavities and sharp

saliences of plaques. The main disadvantages of the geometric snake are the computational effort and the risk of leakage of the active contour. If the errors in the output of the DP algorithm are small, a simple smoothing with a weighted smoothing spline [43,44] should be enough and has the advantage of being faster to compute.

5. Concluding remarks

A new method was proposed for the segmentation of both the near-end and the far-end intima-media regions of the CCA in ultrasound images. The adventitia is detected by searching for the best fit of a cubic spline to edges having features compatible with the adventitia boundary. A global smoothness constraint and discriminating features of the adventitia are used to reduce the attraction by other edges. A smooth estimate of the lumen boundary is obtained from the location of the detected adventitia, using dynamic programming, smooth intensity thresholding surfaces and geometric snakes.

The method was subjected to statistical evaluation, using a set of 47 images from 24 different symptomatic patients, including several classes (II–IV), sizes and shapes of plaques. The results showed that the proposed approach is able to produce segmentations with an accuracy comparable to the manual tracings of medical experts, even for the near-end wall and for arteries with large, hypoechogenic or irregular plaques, problems usually not considered in previous works.

Although manual correction could improve the results, it was not used because one of the main objectives of this work was to reduce user interaction as much as possible.

Despite the promising results, the detection of the lumen boundaries can fail in images with very poor quality, which are common in clinical practice. In many cases, the whole plaque or a significant part of it can only be detected with complementary information, like power-Doppler imaging or other B-scans of the same anatomical region taken from different angles. The medical expert often uses this complementary information to infer the approximate location of the carotid boundaries when they are discontinuous or difficult to detect. Therefore, the integration of this type of complementary data may be necessary for the automatic segmentation of severely degraded images, in order to reduce the automatic detection error to levels comparable to the ones found in manual tracings done by medical experts in current clinical practice. Nevertheless, even without this complementary data, we believe the performance of the algorithm can be improved by relaxing the spline used in the adventitia detection and by using contextual information, taken from the region between each edge and the lumen, to improve the discrimination of edges. This is an interesting topic for future research.

The results can also be improved by enhancing the quality and the precision of the ultrasound images with techniques like pixel compounding [45], if a sequence of images is available.

Another aim for future work is to extend the statistical analysis to a larger set of images.

References

[1] D. O'Leary, J. Polak, R. Kronmal, T. Manolio, G. Burke, S. Wolfson Jr., Carotid-artery intima and media thickness as a risk factor for myocardial infarction and stroke in older adults, New Engl. J. Med. 340 (1999) 14–22.

[2] H. Hodis, W. Mack, L. LaBree, R. Selzer, C. Liu, C. Liu, S. Azen, The role of carotid arterial intima-media thickness in predicting clinical coronary events, Ann. Intern. Med. 128 (4) (1998) 262–269.

[3] R. Kern, K. Szabo, M. Hennerici, S. Meairs, Characterization of carotid artery plaques using real-time compound B-mode ultrasound, Stroke 35 (2004) 870–875.

[4] S.M. Ellis, R.P. Naoumova, C.K. Neuwirth, R. Eckersley, D.O. Cosgrove, G.R. Thompson, P.S. Sidhu, Measurement of the reflectivity of the intima-medial layer of the common carotid artery improves the discriminatory value of intima-medial thickness measurement as a predictor of risk of atherosclerotic disease, Ultrasound Med. Biol. 33 (7) (2007) 1029–1038.

[5] I.M. Graf, F.H.B.M. Schreuder, J.M. Hameleers, W.H. Mess, R.S. Reneman, A.P.G. Hoeks, Wall irregularity rather than intima-media thickness is associated with nearby atherosclerosis, Ultrasound Biol. Med. 35 (6) (2009) 955–961.

[6] D. Baldassarre, M. Amato, A. Bondioli, C.R. Sirtori, E. Tremoli, Carotid artery intima-media thickness measured by ultrasonography in normal clinical practice correlates well with atherosclerosis risk factors, Stroke 31 (2000) 2426–2430.

[7] M. Halenka, Noninvasive measurement of early atherosclerosis by high-resolution B-mode ultrasonography, Acta Univ. Palacki. Olomu. Fac. Med. 142 (1999) 7–12.

[8] R. Rocha, Image Segmentation and Reconstruction of 3D Surfaces from Carotid Ultrasound Images, Ph.D. thesis, Faculdade de Engenharia da Universidade do Porto, Porto (July 2007). <http://www.ineb.fe.up.pt/bmivic>.

[9] A. Gee, R. Prager, G. Treece, L. Berman, Engineering a freehand 3D ultrasound system, Pattern Recogn. Lett. 24 (4–5) (2003) 757–777.

[10] M. Sonka, W. Liang, R. Stefancik, A. Stolpen, Handbook of Medical Imaging: Medical Image Processing and Analysis, SPIE 2 (2000).

[11] Y. Yu, S. Acton, Speckle reducing anisotropic diffusion, IEEE Trans. Image Process. 11 (11) (2002) 1260–1270.

[12] Y. Yu, S. Acton, Edge detection in ultrasound imagery using the instantaneous coefficient of variation, IEEE Trans. Image Process. 13 (12) (2004) 1640–1655.

[13] J.M. Thijssen, Ultrasonic speckle formation, analysis and processing applied to tissue characterization, Pattern Recogn. Lett. 24 (4–5) (2003) 659–675.

[14] C.P. Loizou, C.S. Pattichis, C.I. Christodoulou, R.S.H. Istepanian, M. Pantziaris, A. Nicolaides, Comparative evaluation of despeckle filtering in ultrasound imaging of the carotid artery, IEEE Trans. Ultrason. Fer. Freq. Control 52 (10) (2005) 1653–1669.

[15] K.L. Chan, Ultrasonic tissue characterization using fractal feature, in: IEE Conf. Acoustic Sensing and Imaging, vol. 369, 1993, pp. 183–188.

[16] P.J. Touboul, P. Prati, P.-Y. Scarabin, V. Adrai, E. Thibout, P. Ducimetiere, Use of monitoring software to improve the measurement of carotid wall thickness by B-mode imaging, J. Hypertens. 10 (5) (1992) 37–41.

[17] J. Gariepy, M. Massonneau, J. Levenson, D. Heudes, A. Simon, the Groupe de prevention cardio-vasculaire en medecine du travail, evidence for in vivo carotid and femoral wall thickness in human hypertension, J. Hypertens. 22 (1) (1993) 111–118.

[18] R.H. Selzer, H.N. Hodis, H. Kwong-Fu, W.J. Mack, P.L. Lee, C.R. Liu, C.H. Liu, Evaluation of computerized edge tracking for quantifying intima-media thickness of the common carotid artery from B-mode ultrasound images, Atherosclerosis 111 (1994) 1–11.

[19] T. Gustavsson, Q. Liang, I. Wendelhag, J. Wikstrand, A dynamic programming procedure for automated ultrasonic measurement of the carotid artery, Comput. Cardiol. (1994).

[20] I. Wendelhag, Q. Liang, T. Gustavsson, J. Wikstrand, A new automated computerized analyzing system simplifies readings and reduces the variability in ultrasound measurement of intima-media thickness, Stroke 28 (1997) 2195–2200.

[21] Automatic detection of the intimal and the adventitial layers of the common carotid artery wall in ultrasound Bmode images using snakes, in: International Conference on Image Analysis and Processing, B. Werer, 1999, pp. 452–457.

[22] Q. Liang, I. Wendelhag, J. Wikstrand, T. Gustavsson, A multiscale dynamic programming procedure for boundary detection in ultrasound artery images, IEEE Trans. Med. Imag. 19 (2) (2000) 127–142.

[23] R.H. Selzer, W.J. Mack, P.L. Lee, H. Kwong-Fu, H.N. Hodis, Improved common carotid elasticity and intima-media thickness measurements from computer analysis of sequential ultrasound frames, Atherosclerosis 154 (1) (2001) 185–193.

[24] A. Schmidt-Trucksass, D. Cheng, M. Sandrock, J. Schulte-Monting, R. Rauramaa, M. Huonker, H. Burkhardt, Computerized analysing system using the active contour in ultrasound measurement of carotid artery intima-media thickness, Clin. Physiol. 5 (2001) 561–569.

[25] D. Cheng, A. Schmidt-Trucksass, K. Cheng, H. Burkhardt, Using snakes to detect the intimal and adventitial layers of the common carotid artery wall in sonographic images, Comput. Methods Programs Biomed. 67 (2002) 27–37.

[26] J.H. Stein, C.E. Korcarz, M.E. Mays, P.S. Douglas, M. Palta, H. Zhang, T. LeCaire, D. Paine, D. Gustafson, L. Fan, A semiautomated ultrasound border detection program that facilitates clinical measurement of ultrasound carotid intima-media thickness, J. Am. Soc. Echocardiogr. 18 (3) (2005) 244–251.

[27] C.P. Loizou, C.S. Pattichis, M. Pantziaris, T. Tyllis, A. Nicolaides, Snakes based segmentation of the common carotid artery intima media, Med. Bio. Eng. Comput. 45 (2007) 35–49.

[28] S.D. Yanowitz, A.M. Bruckstein, A new method for image segmentation, Comput. Graph. Image Process. 46 (1989) 82–95.

[29] T. Chan, L. Vese, Active contours without edges, IEEE Trans. Image Process. 10 (2) (2001) 266–277.

[30] L.A. Vese, T.F. Chan, A multiphase level set framework for image segmentation using the Mumford and Shah model, Int. J. Comput. Vision 50 (3) (2002) 271–293.

[31] M.A. Fischler, R.C. Bolles, Random sample consensus: a paradigm for model fitting with applications to image analysis and automated cartography, Commun. ACM 24 (6) (1981) 381–395.

[32] G.W. Zack, W.E. Rogers, S.A. Latt, Automatic measurement of sister chromatid exchange frequency, J. Histochem. Cytochem. 25 (7) (1977) 741–753.

[33] J. Canny, A computational approach to edge detection, IEEE Trans. Pattern Anal. Mach. Intell. 8 (6) (1986) 679–698.
[34] L. Rudin, S. Osher, E. Fatemi, Nonlinear total variation based noise removal algorithms, in: Proceedings of the Eleventh Annual International Conference of the Center for Nonlinear Studies on Experimental Mathematics: Computational Issues in Nonlinear Science, Elsevier North-Holland, Inc., 1992, pp. 259–268.
[35] L. Rudin, S. Osher, Total variation based image restoration with free local constraints, in: Proceedings of IEEE International Conference on Image Processing (ICIP'94), vol. 1, 1994, pp. 31–35.
[36] J.A. Sethian, Level Set Methods and Fast Marching Methods, Cambridge University Press, 1999.
[37] S. Osher, R. Fedkiw, Level Set Methods and Dynamic Implicit Surfaces, Springer-Verlag, New York, 2003.
[38] D. Mumford, J. Shah, Optimal approximations by piecewise smooth functions and associated variational problems, Commun. Pure Appl. Math. 42 (5) (1989) 577–685.
[39] R. Burden, J.D. Faires, Numerical Analysis, Brooks Cole, 2000.
[40] H. Breu, J. Gil, D. Kirkpatrick, M. Werman, Linear time Euclidean distance transform algorithms, IEEE Trans. Pattern Anal. Mach. Intell. 17 (5) (1995) 529–533.
[41] J.M. Bland, D.G. Altman, Statistical methods for assessing agreement between two methods of clinical measurement, Lancet 1 (8476) (1986) 307–310.
[42] C.P. Loizou, C.S. Pattichis, M. Pantziaris, A. Nicolaides, An integrated system for the segmentation of atherosclerotic carotid plaque, IEEE Trans. Info. Tech. Biomed. 11 (6) (2007) 661–667.
[43] C. de Boor, A Practical Guide to Splines, Springer-Verlag, 1978.
[44] M. Unser, Splines: a perfect fit for signal and image processing, IEEE Signal Processing Magazine 16 (6) (1999) 22–38.
[45] Z. Yang, T.A. Tuthill, D.L. Raunig, M.D. Fox, M. Analoui, Pixel compounding: resolution-enhanced ultrasound imaging for quantitative analysis, Ultrasound Med. Biol. 33 (8) (2007) 1309–1319.